

Supporting Information:

Reaction Layer Imaging Using Fluorescence Electrochemical Microscopy

Minjun Yang¹, Christopher Batchelor-McAuley¹, Enno Kätelhön¹, Richard G. Compton¹ (✉)

¹ Department of Chemistry, Physical and Theoretical Chemistry Laboratory, University of Oxford, South Parks Road, Oxford OX1 3QZ, United Kingdom

ABSTRACT

The chemical confinement of a pH sensitive fluorophore to a thin-reaction layer adjacent to an electrode surface is explored as potentially innovative route to improving the spatial resolution of fluorescence electrochemical microscopy. A thin layer opto-electrochemical cell is designed, facilitating the visualisation of a carbon fibre (diameter 7.0 μm) electrochemical interface. Proton consumption is driven at the interface by the reduction of benzoquinone to hydroquinone and the resulting interfacial pH change is revealed using the fluorophore 8-hydroxypyrene-1,3,6-trisulfonic acid. It is demonstrated that the proton depletion zone may be constrained and controlled by the addition of a finite acid concentration to the system. Simulation of the resulting fluorescence intensity profiles is achieved on the basis of a finite difference model, with excellent agreement between the theoretical and experimental results.

Address correspondence to Richard G. Compton, Richard.compton@chem.ox.ac.uk

SI Contents

Section 1: Opto-Electrochemical cell design

Section 2: Microscope filter set

Section 3: Theoretical model

Section 4: Voltammetric response of benzoquinone at a platinum microelectrode

Section 5: Voltammetry of benzoquinone in the absence of buffer

Section 6: Voltammetry of benzoquinone in the presence of buffer

Section 7: Voltammetry of HPTS

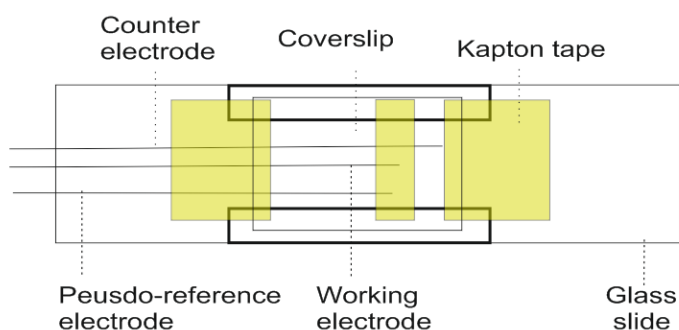
Section 8: Emmision spectra of HPTS

Section 9: Simulated reaction layer profiles

Section 1: Opto-Electrochemical cell design

A schematic of the microscope slide preparation used for combined optical and electrochemical measurements is shown in Figure S1. The working carbon fibre electrode is suspended between the slide and coverslip, such that mass-transport to and from the working electrode can be suitably described using a cylindrical co-ordinate system. The glass slide is 1.0 – 1.2mm in thickness, well beyond the diffusion layer thickness in the experimental time scale.

Top view



Side view

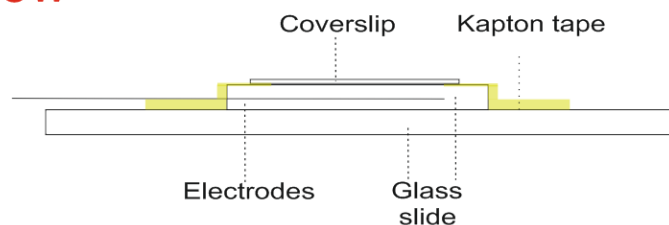


Figure S1: Opto-electrochemical cell design used for imaging the fluorescent images of the reaction layer.

Section 2: Microscope filter set

Figure S2 depicts the excitation and emission bands of the MDF-FITC filter set, data provided by the commercial supplier Thorlabs.

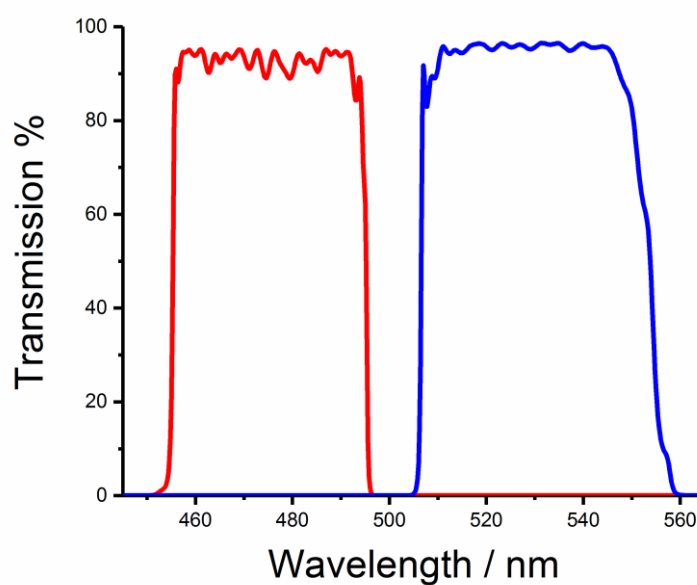
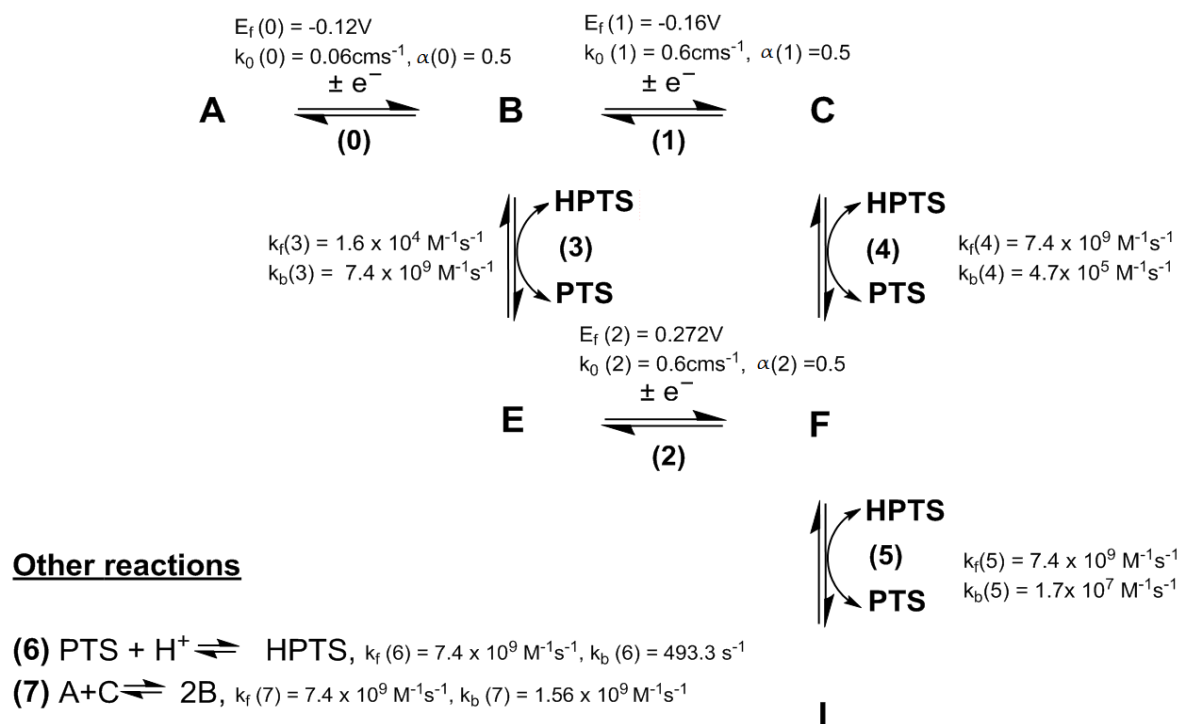


Figure S2: Excitation(red) and emission filters (blue) transmission % for MFD - FITC filter set provided by Thorlabs.

Section 3: Theoretical model



Scheme S1: The ‘half’ scheme of squares used to simulate the concentration profile of PTS that leads to prediction of intensity profile in Figure 8 in the main text.

Finite differences

To simplify the mathematical model and to enable generality of applicability of our results, dimensionless parameters as defined in Table S1 were used in all simulations.

Table S1. Dimensionless parameters, r_e = radius of the electrode, F = Faraday constant, t = time, x = distant from the electrode surface, c_j = concentration of species j , E_f^0 = formal potential, k_0 = electron transfer rate constant, α = transfer coefficient, n = sequential reaction numbering shown in scheme S1.

Parameter	Normalisation
spatial coordinate	$X = x/r_e$
concentration	$C_j = c_j/c_A^*$
diffusion coefficient	$d_j = D_j/D_A$
time	$T = D_A t/r_e^2$
second order rate constant	$K_f^{2nd} = k_f c_A r_e^2 / D_A$ $K_b^{2nd} = k_b c_A r_e^2 / D_A$
potential	$\theta = (F/RT)(E - E_f^0)$
oxidation rate constants	$K_{ox}(n) = k_0(n) e^{(1-\alpha)\theta} r_e / D_A$
reduction rate constants	$K_{red}(n) = k_0(n) e^{-\alpha\theta} r_e / D_A$

This leads to the following equations for the mass transport and homogenous reactions:

$$\begin{aligned}
\frac{\partial C_A}{\partial T} &= d_A \nabla^2 C_A - K_f^{2nd}(7) C_A C_C + K_b^{2nd}(7) C_B^2 \\
\frac{\partial C_B}{\partial T} &= d_B \nabla^2 C_B - K_f^{2nd}(3) C_B C_{HPTS} + K_b^{2nd}(3) C_E C_{PTS} + 2K_f^{2nd}(7) C_A C_C - \\
&2K_b^{2nd}(7) C_B^2 \\
\frac{\partial C_C}{\partial T} &= d_C \nabla^2 C_C - K_f^{2nd}(4) C_C C_{HPTS} + K_b^{2nd}(4) C_F C_{PTS} - K_f^{2nd}(7) C_A C_C + \\
&K_b^{2nd}(7) C_B^2 \\
\frac{\partial C_E}{\partial T} &= d_E \nabla^2 C_E + K_f^{2nd}(3) C_B C_{HPTS} - K_b^{2nd}(3) C_E C_{PTS} \\
\frac{\partial C_F}{\partial T} &= \\
&d_F \nabla^2 C_F + K_f^{2nd}(4) C_C C_{HPTS} - K_b^{2nd}(4) C_F C_{PTS} - K_f^{2nd}(5) C_F C_{HPTS} + \\
&K_b^{2nd}(5) C_I C_{PTS} \\
\frac{\partial C_I}{\partial T} &= d_I \nabla^2 C_I + K_f^{2nd}(5) C_F C_{HPTS} - K_b^{2nd}(5) C_I C_{PTS} \\
\frac{\partial C_{HPTS}}{\partial T} &= d_{HPTS} \nabla^2 C_{HPTS} - C_{HPTS} \left(K_f^{2nd}(3) C_B + K_f^{2nd}(4) C_C + \right. \\
&K_f^{2nd}(5) C_F + K_b^{1st}(6) \left. \right) + C_{PTS} (K_b^{2nd}(3) C_E + K_b^{2nd}(4) C_F + K_b^{2nd}(5) C_I + \\
&K_f^{2nd}(6) C_{H^+})
\end{aligned}$$

$$\frac{\partial C_{PTS}}{\partial T} = d_{PTS} \nabla^2 C_{PTS} + C_{HPTS} \left(K_f^{2nd}(3)C_B + K_f^{2nd}(4)C_C + K_f^{2nd}(5)C_F + K_b^{1st}(6) \right) - C_{PTS} (K_b^{2nd}(3)C_E + K_b^{2nd}(4)C_F + K_b^{2nd}(5)C_I + K_f^{2nd}(6)C_{H^+})$$

$$\frac{\partial C_{H^+}}{\partial T} = d_{H^+} \nabla^2 C_{H^+} - K_f^{2nd}(6)C_{PTS}C_{H^+} + K_b^{1st}(6)C_{HPTS}$$

where $\nabla^2 = (\frac{\partial^2}{\partial X^2} + \frac{1}{X} \frac{\partial}{\partial X})$ for cylindrical geometry and $K_b^{1st}(6) = K_f^{2nd}(6)/c_A^* K_{eq,HPTS}$.

These equations were solved subject to the following boundary conditions at $0 \leq X \leq \infty$, $T=0$ and $X = \infty$, $0 \leq T \leq T_{max}$:

$$C_A, X = [A]_{bulk}$$

$$C_B, X, C_C, X, C_E, X, C_F, X, C_I, X = 0$$

$$C_{HPTS, X, eq} = C_{HPTS} - 2a$$

$$C_{PTS, X, eq} = a$$

$$C_{H^+, X, eq} = a + C_{H^+}$$

where:

C_{HPTS} & C_{H^+} is the concentration of HPTS and HCl added respectively.

$C_{specie, X, eq}$ is the equilibrium concentration of HPTS at distance X away from the electrode surface.

a is the dissociation constant.

$$pK_a(HPTS) = -\log_{10} \left\{ \frac{C_{PTS, eq} C_{H^+, eq}}{C_{HPTS, eq}} \right\} = -\log_{10} \left\{ \frac{a^2}{C_{HPTS} - 2a} \right\}$$

m

The rate constants for oxidation and reduction were described by the Butler-Volmer model.

For $x = 0$, $t > 0$ we considered the boundary conditions:

$$d_A \left(\frac{\partial C_A}{\partial X} \right)_{X=0} = K_{red}(0)C_A(0, t) - K_{ox}(0)C_B(0, t)$$

$$d_B \left(\frac{\partial C_B}{\partial X} \right)_{X=0} = -K_{red}(0)C_A(0, t) + K_{ox}(0)C_B(0, t) + K_{red}(1)C_B(0, t) -$$

$$\begin{aligned}
& K_{ox}(1)C_C(0, t) \\
& d_C \left(\frac{\partial C_C}{\partial X} \right)_{X=0} = -K_{red}(1)C_B(0, t) + K_{ox}(1)C_C(0, t) \\
& d_E \left(\frac{\partial C_E}{\partial X} \right)_{X=0} = K_{red}(2)C_E(0, t) - K_{ox}(2)C_F(0, t) \\
& d_F \left(\frac{\partial C_F}{\partial X} \right)_{X=0} = -K_{red}(2)C_E(0, t) + K_{ox}(2)C_F(0, t)
\end{aligned}$$

$$\begin{aligned}
& \frac{\partial C_I}{\partial X} = 0 \\
& \frac{\partial C_{HPTS}}{\partial X} = 0 \\
& \frac{\partial C_{PTS}}{\partial X} = 0 \\
& \frac{\partial C_{H^+}}{\partial X} = 0
\end{aligned}$$

Coupled mass-transport and reaction equations were solved via the finite difference method. To this end, partial differential equations were discretised using a uniform temporal grid and a spatial grid expanding from the electrode surface to:

$$X_{max} = 1 + 6\sqrt{T_{max}}$$

where T_{max} is the dimensionless duration of the experiment and X_{max} is a dimensionless distance defined well beyond the thickness of the diffusion layer around the electrode (see Table S1 for dimensionless parameters). The simulations were developed in C++ and ran on an Intel (R) Core (TM) i5-3570 CPU 3.40 GHz PC with 4.00 GB RAM, with a typical run time of approximately 1 hour.

The simulation was tested¹ extensively via a number of different approaches. Conducted trials included the measurement of the entire mass and total flux at any point in time to ensure its conservation. Two simulations at lower accuracy, i.e. at a greater grid- and time spacing and at a finer grid expansion factor, gave the exact result ensuring convergence. The simulation results were further compared with

data obtained via the commercial package DIGISIM.

Section 4: Voltammetric response of p-benzoquinone at a platinum microelectrode

The reduction of benzoquinone (1mM) was studied at a platinum micro-disc electrode (radius = 55 μm) in an aqueous and non-buffered 0.10 M KCl solution. Figure S3 depicts the near steady-state reduction process occurring at -0.20 V vs SCE. Microelectrodes can be distinctly beneficial for the measurement of diffusion coefficients.^{2 3} At a macro-electrode the peak current is first, proportional to the square-root of the diffusion coefficient and second, sensitive to the electron transfer kinetics. This can lead to significant errors in determination of a species diffusion coefficient.

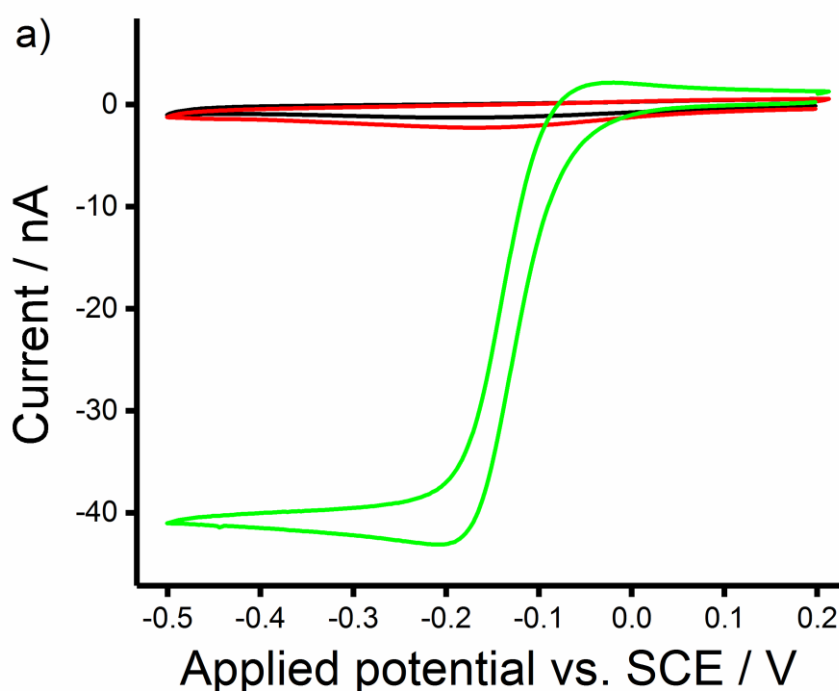


Figure S3: Cyclic voltammetry of 1.0mM BQ in a degassed 0.10M KCl supporting electrolyte solution at a 55 μm radius Pt electrode. Green – 1.0mM BQ, Black - control, red - 1minute immerse in 1.0mM BQ solution and rinse.

Figure S4, depicts the chronoamperometric response of the same electrochemical system to a potential step to -0.25 V vs SCE. Attempts to analyse the short-time response of the system using the Shoup-Szabo equation were unsuccessful. This lack

of fit was ascribed as being due to adsorption of the quinone to the platinum surface.
⁴ This adsorption was further evidenced in Figure S3 where exposure of the electrode to a 1.0 mM BQ solution prior to immersion and recording of the cyclic voltammetry lead to the observation of a small reductive peak at -0.16 V vs SCE (red line Figure S3).

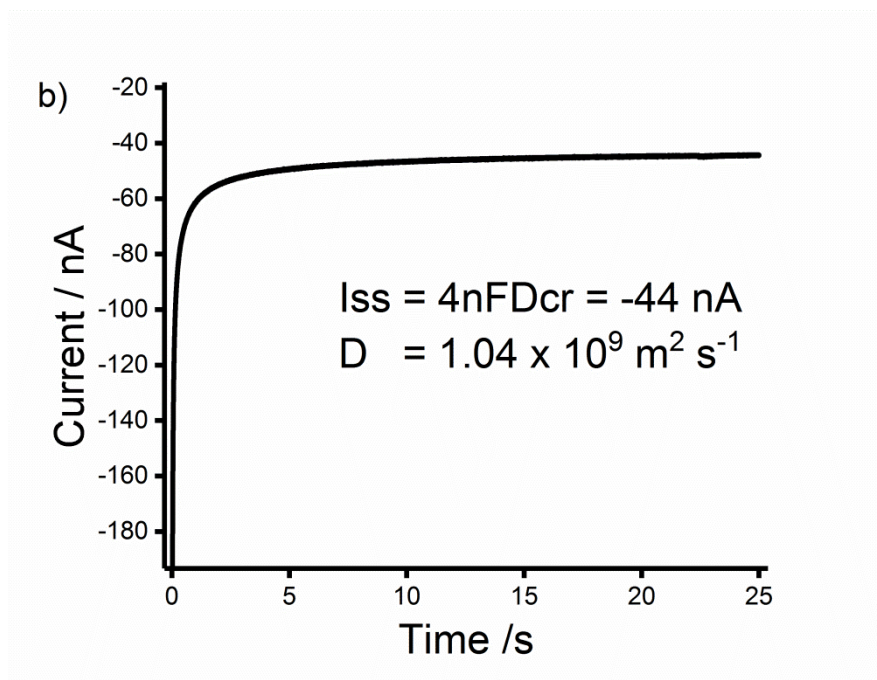


Figure S4: Chronoamperometric response of 1.0mM BQ with 0.10M KCl supporting electrolyte degassed on a 55um radius Pt electrode, with the potential stepped to -0.25V vs SCE at $t = 0$ s.

From the measured steady-state current the diffusion coefficient for the benzoquinone was determined to be $1.04 \pm 0.05 \times 10^{-9} \text{ m}^2 \text{ s}^{-1}$ at 298 K.

Section 5: Voltammetry of p-benzoquinone in the absence of buffer

Using the the coefficient measured in the previous section we are now in a able to consider the voltammetric response of p-benzoquinone at a glassy carbon macroelectrode. Figure 1 in the main text depicts the reduction process as a function of scan rate; a single redox wave is observed at -0.177 V vs SCE. We highlight that under non-aqueous conditions the difference in potential between the first and second electron transfer is of the order of one volt, this likely arises due to the coulombic repulsion between the first and second electron transfer. However, due to hydrogen bonding in the aqueous environment this difference in potentials is significantly compressed. First, using the measured diffusion coefficient we consider if the voltammetric wave is a one or two electron process.

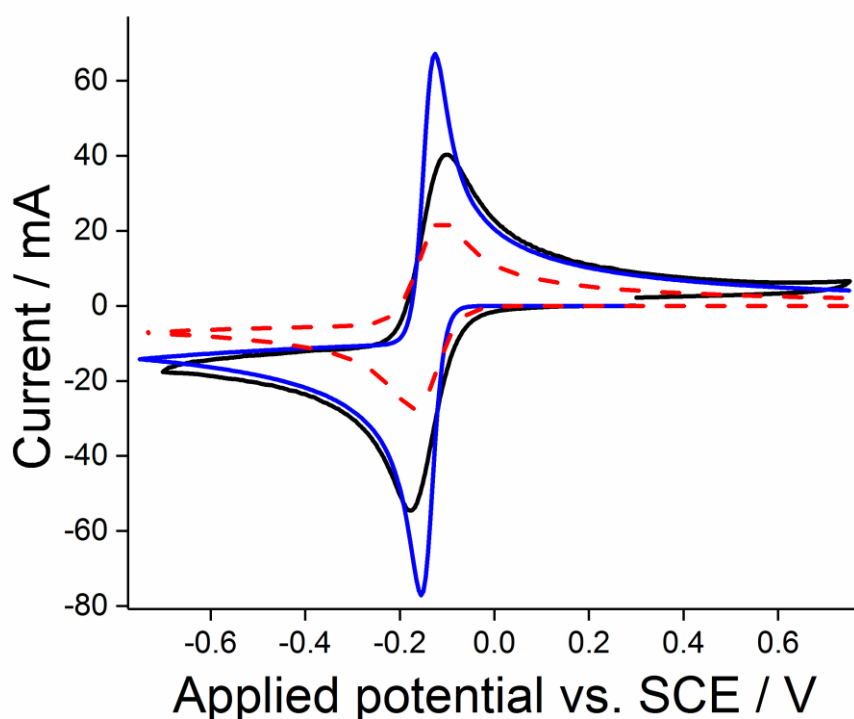


Figure S5: Blue line - Digisim^{5 6 7 8} simulated CV for $A + 2e = C$, with $E_f = -0.14V$, $a = 0.5$, $D_{A \& B} = 1.04 \times 10^{-9} m^2 s^{-1}$, $r = 1.5mm$. Black line – CV of 1mM BQ with 0.1M KCl supporting electrolyte recorded on an unmodified glassy carbon electrode degassed at a scan rate of $200 mVs^{-1}$.

Figure S5 depicts the experimentally recorded voltammetry for the reduction of p-

benzoquinone (1.0mM) in a 0.10 M KCl solution at 200 mV s⁻¹. Overlaid is the simulated response for a reversible one and two-electron transfer, where in the latter case the second electron has been considered to be highly driven. As can be seen the experimental peak current lies between these two limits. However, as the wave is larger than that predicted for a one-electron transfer it must be concluded that more than one-electron is being transferred during the reduction process. Furthermore, changes in the peak current in consecutive redox cycles of p-benzoquinone are negligible, hence the electron transfer in Figure S5 is assumed to be fully reversible. However, we note that relaxation of this reversibility constraint does not in itself lead to a satisfactory fit between the experimental and simulated results.

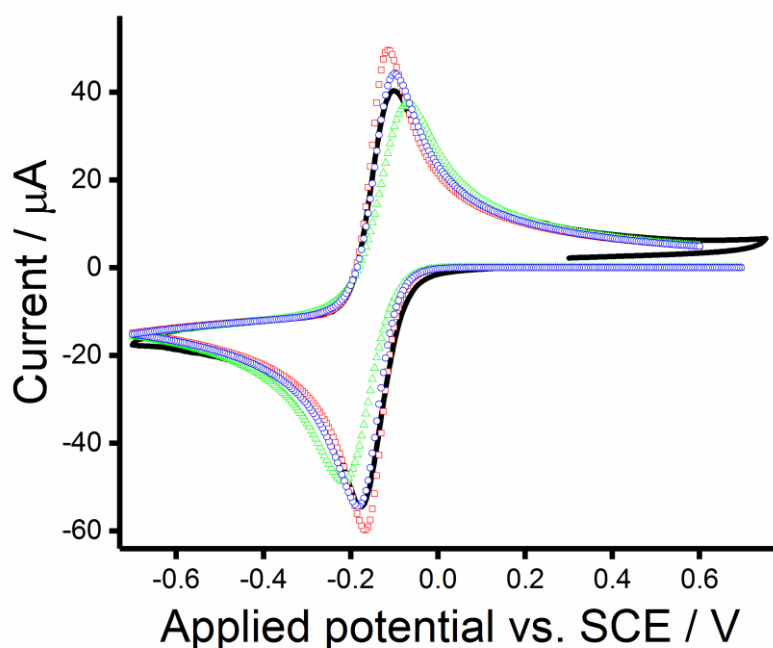


Figure S6: Digisim simulated CV for $A + e = B$ (1) & $B + e = C$ (2), with $E_f(1\&2) = -0.14V$, $a = 0.5$, $D_{A\&B} = 1.04 \times 10^{-9} m^2 s^{-1}$, $r = 1.5mm$. Red square - $k_0(1\&2) = 0.06 cm s^{-1}$, blue circles - $k_0(1\&2) = 0.015 cm s^{-1}$ and green triangles - $k_0(1\&2) = 0.005 cm s^{-1}$. Black line – CV of 1mM BQ with 0.10M KCl supporting electrolyte recorded on an unmodified glassy carbon electrode degassed at a scan rate of 200mVs⁻¹.

Figure S6 depicts the simulated response for a two electron transfer process in which the first and second electron are assumed to have the same formal potential; the second electron transfer is not assumed to be “highly driven”. In this situation, although the redox wave is overall still a two-electron process the peak height is

significantly diminished. This decrease in the peak-height reflects the finite possibility of the electroactive species diffusing away from the surface after only one electron has been transferred. In comparison to the experimental data in this model, in which the first and second electron transfer are considered to occur at similar potentials but step wise, provides a far better physical description of the data. Figure S6 also shows how the predicted voltammetric response varies as the rate of electron transfer is reduced from being reversible to quasi-irreversible. Although relaxation of the reversibility of the processes enables the magnitude of the forward peak current to be aptly described, a small discrepancy in the magnitude of the simulated and experimental peak height is observed. This can be further improved by assuming that the second electron transfer is *marginally* less thermodynamically favorable than the first.

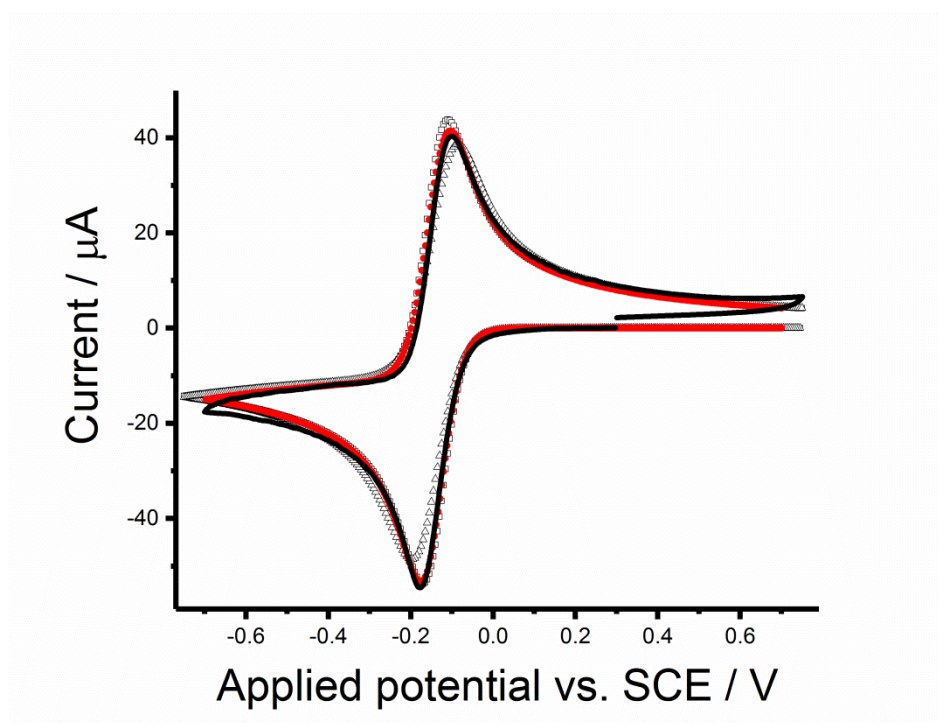


Figure S7: Digisim simulated CV for $A + e = B$ (1) & $B + e = C$ (2), $E_f(1) = -0.12V$, $E_f(2) = -0.16V$, $a = 0.5$, $D_{A \& B} = 1.04 \times 10^{-9} m^2 s^{-1}$ and $r = 1.5 mm$. Square $k_0 = 1 cms^{-1}$, red circles $k_0 = 0.06 cms^{-1}$, triangles $k_0 = 0.01 cms^{-1}$. Black line – CV of 1.0 mM BQ with 0.10 M KCl supporting electrolyte recorded on an unmodified glassy carbon electrode degassed at a scan rate of $200 mVs^{-1}$.

Figure S7 depicts the simulated response where the formal potential for the second electron transfer is 40 mV more negative than the first. Assuming the electron

transfer is set to be greater than 0.06 cm s^{-1} (i.e. effectively reversible) excellent correspondence between the simulated and experimental results are found. Figure 1 of the main article presents the comparison between this simulated model with the experimental data across the full scan rate range. It is on the basis of the above discussion that the formal potentials for the first and second electron transfer are reported to be -0.12 V and $-0.16 \text{ V} \pm 0.001 \text{ V}$ vs SCE respectively.

Section 6: Voltammetry of p-benzoquinone in the presence of buffer

Figure 2 of the main article depicts the voltammetric response of benzoquinone in the presence of a pH 6.3 and pH 2.0 buffer. Under these conditions a marked increase in the peak-to-peak separation is observed. Figure S8 presents the known thermodynamic parameters associated with the benzoquinone reduction process.

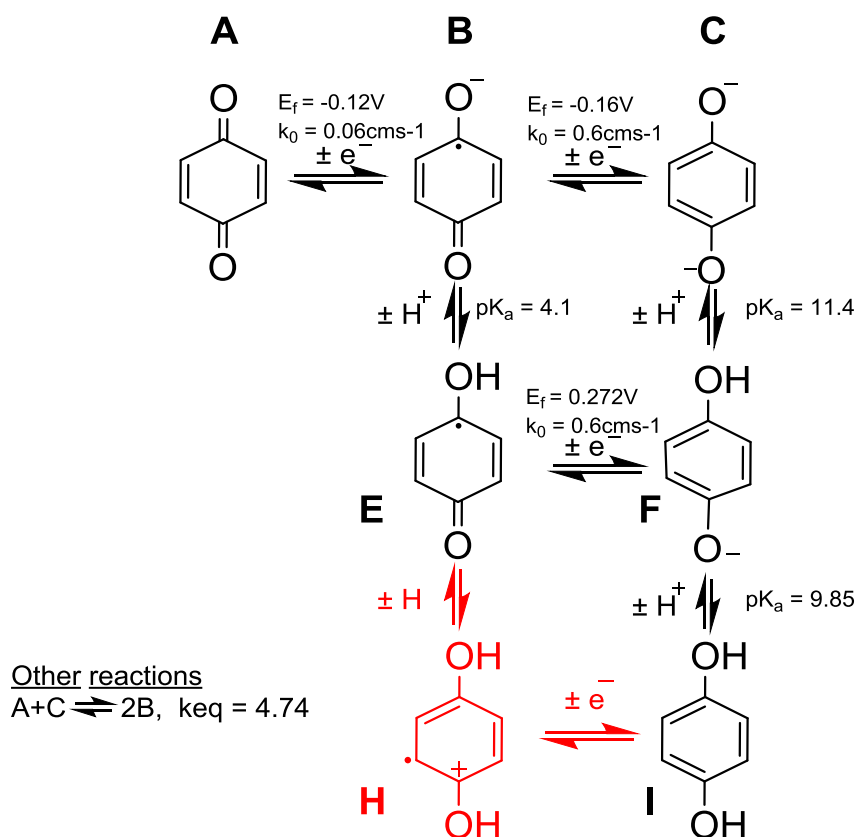


Figure S8: Mechanistic summary of the known thermodynamic information relating to the benzoquinone/hydroquinone redox couple.

The above mechanistic scheme can be used to predict the voltammetric response for the reduction of benzoquinone in a pH 6.3 buffer solution, the results of which and the comparison to the experimental data are depicted in Figure S9.

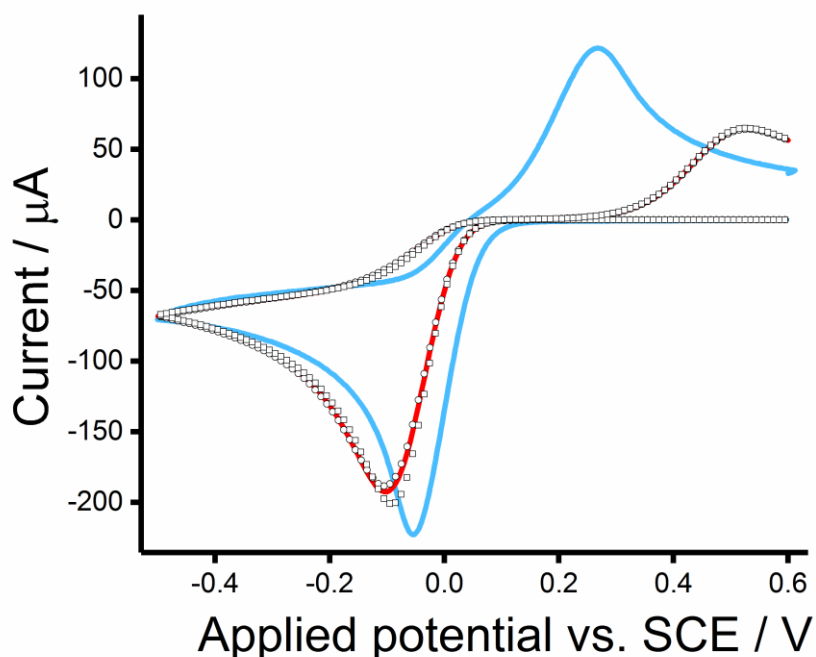


Figure S9: Light blue - CV of 1.0mM BQ in pH 6.3 PBS with 0.10M KCl supporting electrolyte, degassed. Digisim simulated CV of half scheme of square (Figure S8) varying $k_0(EF)$, squares- $k_0(EF) = 6 \text{ cm s}^{-1}$, red line - $k_0(EF) = 0.6 \text{ cm s}^{-1}$ and circles - $k_0(EF) = 0.06 \text{ cm s}^{-1}$.

As can be seen the provided mechanistic scheme is capable of reasonably describing the reduction process however it predicts the overall process to be significantly more irreversible than is found experimentally. This irreversibility does not arise from the electron transfer kinetics being sluggish but in the simulation model the oxidation of the formed hydroquinone becomes chemically gated by the requirement to deprotonate (i.e. below pH 9.85 the hydroquinone remains protonated and in the present scheme it cannot be oxidized in this form). Due to the inherent limitations to this model it is tempting to provide an alternate pathway via which the oxidation process may occur. As marked on the scheme in Figure S8 in red an initially plausible route would be the direct oxidation of the hydroquinone followed by a subsequent deprotonation step. Given that the overall thermodynamics of the conversion of hydroquinone to the mono-deprotonated semiquinone are already known then the formal potential for the proposed oxidation and the associated pK_a are non-independent parameters. Table S2 presents the possible combinations for the

associated pK_a and formal potential.

Table S2. The calculated values of E_0 and pK_a values for the pathway shown in red involving specie H in Figure S8.

E_f/V vs SCE	pK _a
1.5	-10.9
1.0	-2.5
0.5	6.0
0.0	14.4
-0.5	22.9
-1.0	31.4
-1.5	39.8

The formal potential responsible for the early oxidative peak in Figure S9 should be around 0.10V vs SCE. The pK_a values for most compounds normally decreases in value upon successive protonation. However, the pK_a value corresponding to formal potential of 0.10 V (~13) is higher than that of semiquinone (4.1), indicating that the step wise oxidation is likely none operative. There is a possibility of a concerted pathway for the oxidation of hydroquinone but the mechanism proposed in Figure S8 is sufficient to describe the reduction process that happens in the chronoamperometry experiment.

Section 7: Voltammetry of HPTS

The oxidation of HPTS was studied at a glassy carbon macro-electrode, Figure S10. As shown in Figure 4 of the main text a reversible one-electron transfer process occurs at 0.405 V, at higher over potentials a second irreversible oxidative feature is observed. Figure S10 depicts the first (light blue) and second (dark blue) scan of the oxidative process. After oxidation a new feature appears at $\sim 0.0\text{V}$ vs SCE. After the second oxidative process it is proposed that the formed cation undergoes rapid hydrolysis to form a catechol moiety. The formed catechol results in the appearance of the new redox wave situated at $\sim 0.0\text{V}$ vs SCE.

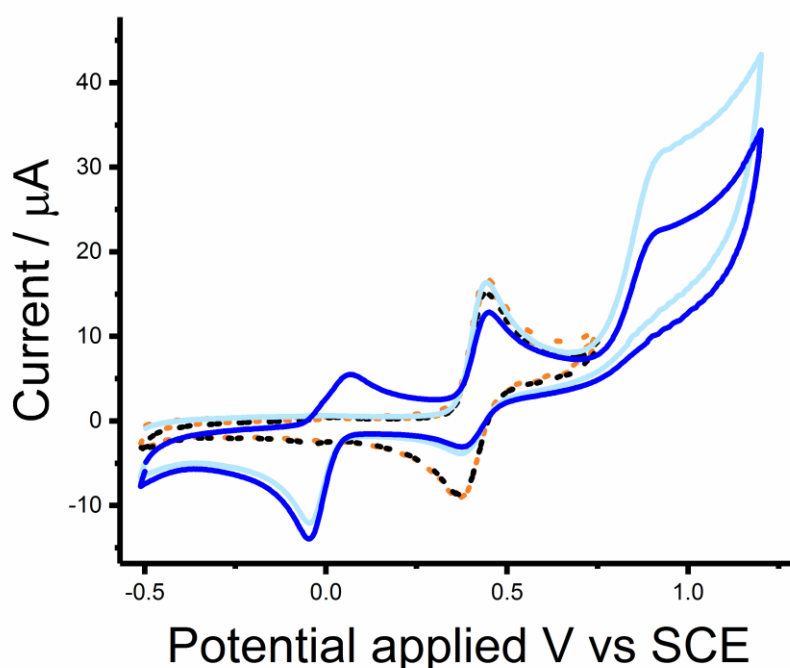


Figure S10: Cyclic voltammetry of 1.0mM HPTS in pH 7.5 PBS degassed aqueous solution containing 0.10M KCl. The dotted line - potential range from -0.50V to 0.75V, first cycle - orange and second cycle - black. The solid line - potential range from 0.50V to 1.20V, first cycle - light blue and second cycle - blue.

Section 8: Emission spectra of HPTS

Figure S11 presents the fluorescence emission spectra for HPTS as a function of the solution phase pH using an excitation wavelength of 454 nm. The excitation at 454 nm corresponds to the absorption maxima for the deprotonated species. As can be seen the magnitude of the emission peak shows a clear correlation with the solution phase pH.

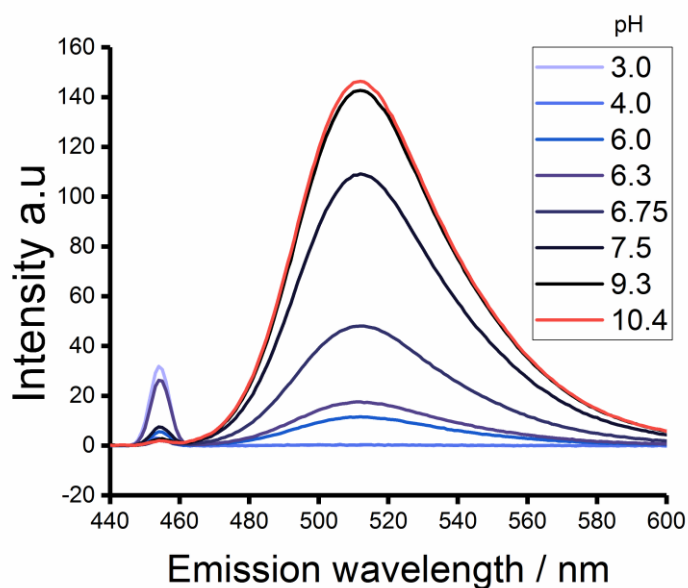


Figure S11: Fluorescence emission spectrum of 10.0 μM HPTS varying pH in 0.10M KCl with excitation wavelength of 454nm.

Section 9: Simulated reaction layer profiles

Figure S12 presents the simulated concentration profile of HPTS, PTS and protons as a function of distance away from the electrode surface. The PTS concentration profile was integrated over all space to determine its projection on a plane parallel to the orientation of the cylindrical electrode and hence to form a simulated proportional intensity profile for comparison with experimental data as presented in the main figure 8.

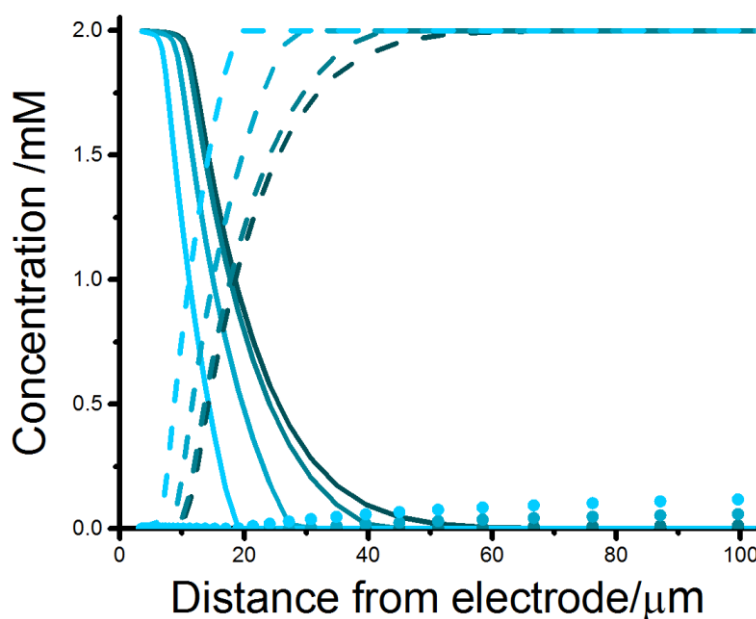


Figure S12: Simulated concentration profile of the HPTS species and protons at $t = 0.5s$ with a different concentration of HCl in C++, potential was step to $-0.6V$ at $0s$. Solid line shows concentration profile of PTS, dotted line represents HPTS and circles for protons. The concentration of HCl added is 0.00, 0.02, 0.07 and 0.14mM from black to light blue.

References

- (1) Kätelhön, E.; Compton, R. G. *Analyst* **2015**, *140*, 2592-2598.
- (2) Wang, Y. J.; Limon-Petersen, J. G.; Compton, R. G. *J. Electroanal. Chem.* **2011**, *652*, 13-17.
- (3) Wang, Y. J.; Rogers, E. I.; Compton, R. G. *J. Electroanal. Chem.* **2010**, *648*, 15-19.
- (4) Pang, K. P.; Benziger, J. B.; Soriaga, M. P.; Hubbard, A. T. *J. Phys. Chem.* **1984**, *88*, 4583-4586.
- (5) Rudolph, M. *J. Electroanal. Chem.* **1991**, *314*, 13-22.
- (6) Rudolph, M. *J. Electroanal. Chem.* **1992**, *338*, 85-98.
- (7) Rudolph, M. *J. Electroanal. Chem.* **1994**, *375*, 89-99.
- (8) Rudolph, M.; Reddy, D. P.; Feldberg, S. W. *Anal. Chem.* **1994**, *66*, A589-A600.